RSC Advances

Cite this: DOI: 10.1039/c0xx00000x

www.rsc.org/xxxxxx

ARTICLE TYPE

Molten salt synthesis of tin doped hematite nanodiscs and their enhanced electrochemical performance for Li-ion batteries

Rencheng Jin,[a]* LiXia Yang,[a] Guihua Li,[a] and Gang Chen[b]

Received (in XXX, XXX) Xth XXXXXXXXX 20XX, Accepted Xth XXXXXXXXX 20XX
DOI: 10.1039/b000000x

Sn^{4+} doped Fe_2O_3 (hematite) nanodiscs have been synthesized by a facile mixed molten salt method. The structure, morphology and compositions of the products are characterized by X-ray diffraction (XRD), filed emission scanning electron microscope (FESEM), transmission electron microscopy (TEM), X-ray photoelectron spectrometer (XPS) and inductively coupled plasma (ICP). According to the time dependent experimental results, the formation mechanism of the Sn^{4+} doped Fe_2O_3 nanodiscs is discussed. The electrochemical properties of the Fe_2O_3 nanodiscs as an anode material are investigated in terms of their reversible capacity, and cycling performance for lithium ion batteries. The Sn^{4+} doped Fe_2O_3 nanodiscs (5% Sn) exhibit a reversible capacity of 899 mAh g^{-1} at a current density of 100 mA g^{-1} after 100 cycles. Even at 1000 mA g^{-1}, the reversible capacity of the nanodiscs still remains 490 mAh g^{-1}. The improved electrochemical performance is ascribed to the introduction of Sn element, which decreases charge transfer resistance, enhances Li ion diffusion velocity, and thus improves its cycling and high-rate capability. These results suggest the promising application of the Sn^{4+} doped Fe_2O_3 nanodiscs in lithium ion batteries.

1. Introduction

Nowadays, Lithium-ion secondary batteries (LIBs) are widely required in industrial and civil applications. However, the graphite currently used as commercial LIBs has low theoretical capacity (372 mAh g-1),[1] which can not fully meet the requirement for batteries with high energy density. Therefore, exploring new anode materials with high performance to replace graphite is of importance for the development of LIBs. Transition metal oxides such as NiO,[2] CoO,[3, 4] SnO,[5-7] FeO[8] have attracted intense attention as promising anode materials for the next generation of LIBs due to their high capacities of 2-3 times higher than that of graphite. Unfortunately, these anode materials generally suffer from a rapid capacity fading due to the large volume changes and stresses during the conversion reactions and/or the low electronic conductivity. To solve these problems, many strategies including morphology modification,[7-10] doping foreign ions,[11, 12] formation carbon or graphene composites[13-16] and surface engineering[17-19] are carried out. Among them, doping foreign ions is more suitable and promising for the practical application of LIBs.

Among those transition metal oxides, iron oxides of Fe_3O_4 and Fe_2O_3 are considered to be promising anode materials because of their advantages of low cost, abundant resource, environmental friendliness, high theoretical capacities.[20-24] However, they are still hindered by their poor cycling performance. To improve the cycling stability of the iron oxide electrodes, different methods such as forming composites with carbon materials,[25-27] synthesizing nanostructured iron oxides (nanoparticles,[28] nanorods,[20] nanowires,[29] nanotubes,[30, 31] nanoplates[32, 33] and nanodiscs[34]) are performed. Although there are many reports on the synthesis and electrochemical properties of iron oxides, less work has been focused on the synthesis and electrochemical properties of foreign ions doped iron oxides.[31]

Molten salt method, a one-pot, low cost, and envirmental benign method, has been widely used to prepare various metal oxides including Fe_2O_3,[35] CuO,[36] Co_3O_4,[37] SnO_2,[38] TiO_2,[39] $ZnCO_2O_4$,[40] $CuCo_2O_4$[41] and etc. Compared to other synthesis method, molten salt method is amenable to large-scale synthesis and the salt(s) can be recovered for re-use. In addition, no toxic reagent/surfactant was used in this method. Here in this work, we report a facile molten salt route to synthesize Sn^{4+} doped Fe_2O_3 nanodiscs in a mixed salt of NaCl: KCl. As expected, the as-prepared Sn^{4+} doped Fe_2O_3 nanodiscs exhibited high reversible capacity, good cycling stability, and high rate capability. In addition, the formation mechanism of Sn^{4+} Fe_2O_3 nanodiscs was proposed according to the time dependent experimental results.

2. Experimental Section

2.1. Preparation of Sn^{4+} doped Fe_2O_3 nanodiscs

All the chemicals were of analytical grade and used without further purification. In the typical procedure, 0.808 g of $Fe(NO_3)_3$, different amount of $SnCl_4$, and 10 g of mixed salts (the mass ratio of NaCl/KCl is equal to 5/5, which is the ratio of its eutectic point) were added in the agate mortar and grinded for 45 min. Then the mixed precursor was placed in an alumina crucible and held in a box furnace at 550 °C for 8 h. After the molten salt reaction, the alumina crucible was cooled down naturally to room temperature. Then the mixed salts were removed by washing with distilled water for several times. The brick red samples were collected and dried in a vacuum at 80 °C for 12 h.

2.2. Characterization

The obtained products were characterized by X-ray diffraction (XRD) on a Rigaku D/Max-2550pc powder diffractometer equipped with Cu Kα radiation (λ=1.54Å, scanning rate=4° min^{-1}). The morphology of the samples was detected by field emission scanning electron microscopy (FESEM, FEI Quanta 200F) and transmission electron microscopy (TEM, FEI Tecnai G2 S-Twin). The X-ray photoelectron spectrometer (XPS) was performed on Axis Ultra Photoelectron Spectrometer with an excitation source of Mg-Al radiation. The composition of the product was characterized by inductively coupled plasma (ICP, NexION 300, America).

2.3. Electrochemical Measurement

The electrochemical tests of the as-prepared samples were carried out using coin-type cells assembled in an argon-filled glove box. A composite electrode was prepared by mixing Fe_2O_3 nanodiscs, polyvinylidene fluoride (PVDF), and carbon black with weight ratio of 70:15:15 in n-methyl pyrrolidinone (NMP) solvent. After stirring the mixture for 6 h, the homogenous slurry was spread uniformly on copper foil substrates by the doctor blade technique and then the electrode was dried in a vacuum at 120 °C overnight. The metallic lithium was used as the counter/reference electrode, a mixture of 1 M LiPF6 in ethylene carbonate and dimethyl carbonate (1: 1 weight) as the electrolyte and the Celgard 2400 film as the separator. Charge-discharge measurements were performed on NEWWARE battery test system at different current density over a voltage range of 0.01 to 3 V. The electrochemical impedance behavior of the electrodes was carried out on CHI660C electrochemical workstation (0.1V).

3. Results and discussion

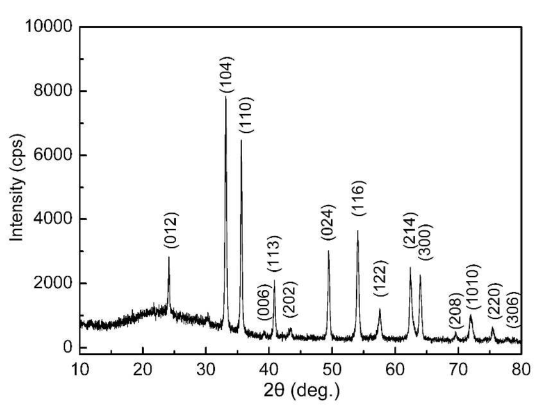

Fig.1 XRD pattern of Sn^{4+} doped Fe_2O_3 nanodiscs obtained at 550 °C in the mixed molten salt.

The XRD pattern of the product obtained at 550 °C (mole ration, Fe/Sn=1.9 mmol/0.1 mmol) is shown in Fig.1, all the diffraction peaks match well with rhombohedral Fe_2O_3 (JCPDS No. 33-0664). No other peaks such as SnO_2 can be detected, demonstrating that the prepared product is pure. The FESEM images of the as-synthesized Sn^{4+} doped Fe_2O_3 structure are presented in Fig. 2. The products consist of numerous nanodiscs, and some nanoparticles can be occasionally observed (Fig. 2a). The nanodiscs are about 400 nm in diameter and ~100 nm in thickness as illustrated in Fig. 2b. Energy dispersive X-ray spectrometer (EDS) measurement reveals that three elements Fe, Sn, O with mole ratio of 52.1: 1.8: 42.4 exist in the products (Fig. S1). This indicates that Sn^{4+} ions can be doped in the Fe_2O_3 nanodiscs. The TEM analysis further reveals that the obtained products are composed of nanodiscks with the diameter of about 400 nm (Fig. 2c). The corresponding selected area electron diffraction (SAED) pattern in the inset of Fig. 2d shows an array of spots with a sixfold rotational symmetry, which indicates the single crystalline of the Sn^{4+} doped nanodiscs. The high crystallinity of the present Fe_2O_3 can be obviously observed from the high resolution TEM (HRTEM) image in Fig. 2d. The lattice fringes of nanocrystalline can be seen clearly from the HRTEM image with a spacing of about 0.251 nm, corresponding to the interplanar distance of (110) crystal planes of the Fe_2O_3. Considering the HRTEM and the SAED pattern of the Fe_2O_3 nanodiscs, the most exposed facet of the Fe_2O_3 nanodiscs is the (001) facet.

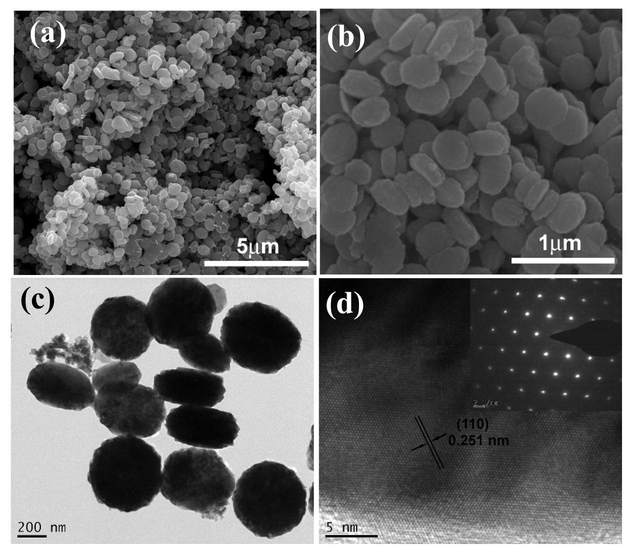

Fig. 2 FESEM images at low (a) and high (b) magnification of the Sn^{4+} doped Fe_2O_3 nanodiscs obtained at 550 °C in the mixed molten salt, (c) TEM image of the obtained Sn^{4+} doped Fe_2O_3 nanodiscs, (d) HRTEM image from the edge of the Sn^{4+} doped Fe_2O_3 nanodiscs, inset: the corresponding SAED pattern of the single Sn^{4+} doped Fe_2O_3 nanodisc.

In order to reveal the surface chemical compositions and the valence states of various species of obtained samples, the XPS analysis was performed. The full XPS spectrum in Fig. 3a confirms that the obtained sample contains elements of Fe, O, Sn and adventitious C. Fig. 3b shows the high resolution spectra of Fe 2p for Sn^{4+} doped Fe_2O_3. The binding energy peak at 710.8 eV corresponds well with Fe 2p3/2, and the binding energy peaks at 724.4 and 719.2 eV are in agreement with the Fe 2p1/2 and the shake-up satellite structure, respectively. The observed values for the binding energy are close to the reported value of Fe^{3+}, which matches well with previous literature.[42] As presented in Fig. 3c, the peaks at binding energy of 487.1 eV and 495.5 eV can be attributed to Sn 3d5/2 and Sn 3d3/2, respectively. The binding energy for Sn 3d5/2 centered around 487.3 eV revealed that the tin was in the Sn^{4+} state.[43] This indicates that tin element can be doped in the Fe_2O_3 nanodiscs. In addition, the spectrum of O 1s in Fe_2O_3 shows three peaks with binding energies at 530.2 eV, 532.2 eV, and 533.4 eV, respectively.[42]

To further investigate Sn^{4+} doped Fe_2O_3, the XRD patterns of samples with different amount of Sn^{4+} were carried out. When no $SnCl_4$ was added in the reaction system, pure Fe_2O_3 was obtained (Fig. 4a). When the mole ratio of Sn/Fe was equal to 0.08, SnO_2 (JCPDS No. 41-1445) was fabricated except the Fe_2O_3. The enlarged XRD pattern shown in Fig. 4b demonstrated that the diffraction spectra for Fe_2O_3 crystals shift to smaller 2θ angles compared to those for pure Fe_2O_3. The result further proved that the Sn^{4+} ions could be doped in Fe_2O_3 nanodiscs. It should point out that the morphology of products was not changed when Sn^{4+} was added in the reaction system. The elemental contents of Fe and Sn of all the samples detected by inductively coupled plasma (ICP) are shown in Table 1. The atomic ratios of Fe to Sn are close to the rate of charge.

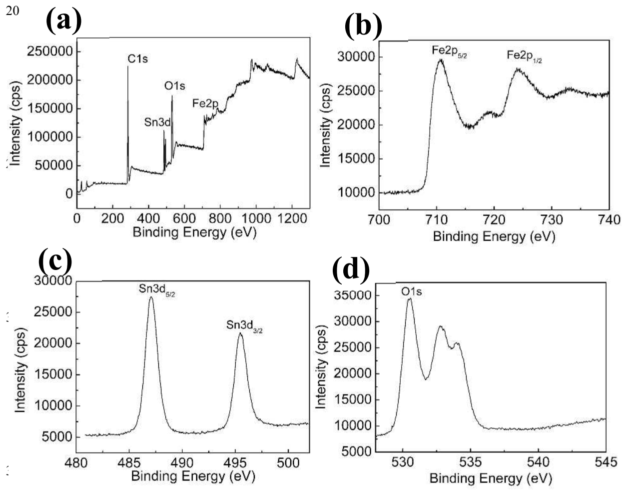

Fig. 3 XPS spectra for (a) survey, (b) Fe 2p, (c) Sn 3d, (d) O 1s of the Sn^{4+} doped Fe_2O_3 nanodiscs.

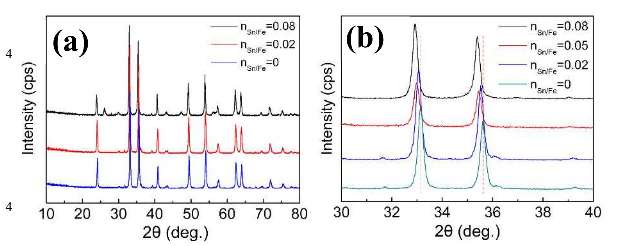

Fig. 4 XRD patterns of the products obtained with addition of different amount of Sn.

A series of time-dependent experiments were performed in order to understand the formation process of Sn^{4+} doped Fe_2O_3 nanodiscs. The samples collected at different time intervals were examined by FESEM. As shown in Fig. 5a and b, some irregular thinner nanodiscs with rough surfaces formed after reaction for 2 h. And some nanoparticles can be observed. After reaction for 4 h, the nanoparticles decreased individually and the nanodiscs became more regular. Simultaneously, the thickness of the nanodiscs increased, as can be seen in Fig. 5c. When the reaction time was further prolonged to 6 h, almost all the irregular nanoparticles disappeared with further increasing the thickness of the Sn^{4+} doped Fe_2O_3 nanodiscs (Fig. 5d). According to the above experimental results and analysis, the whole morphology evolution process of the Sn^{4+} doped Fe_2O_3 nanodiscs is proposed. Such a process involves a fast nucleation of primary particles

Table 1 Composition of the Sn^{4+} Fe_2O_3 nanodiscs obtained with addition of different amount of Sn.

Sample	Rate of charge (Fe:Sn, mmol)	Fe : Sn
A	2:0.04	1:0.021
B	1.9:0.1	1:0.046
C	1.8:0.15	1:0.081

accompanied by an oriented attachment and Ostwald ripening process. The hematite crystal has a rhombohedrally centered hexagonal structure of the corundum type with a close-packed lattice in which two thirds of the octahedral sites are occupied by Fe3+ ions.[34] Compared with other planes of (100), (110), (012), (104), the (001) planes of Fe_2O_3 have the larger packing density. As we know, the close-packed facets are considered as the most stable facets for different types of crystals, and also tend to be the most exposed facets of the crystals in many cases. Therefore, the oriented growth of Fe_2O_3 nanodiscs is of thermodynamically preferred. And the Ostwald ripening can not be omitted. As the Ostwald ripening process proceeds, the smaller nanoparticles adsorbed around the Fe_2O_3 nanodiscs are consumed and grew gradually to make the nanodiscs much thicker.

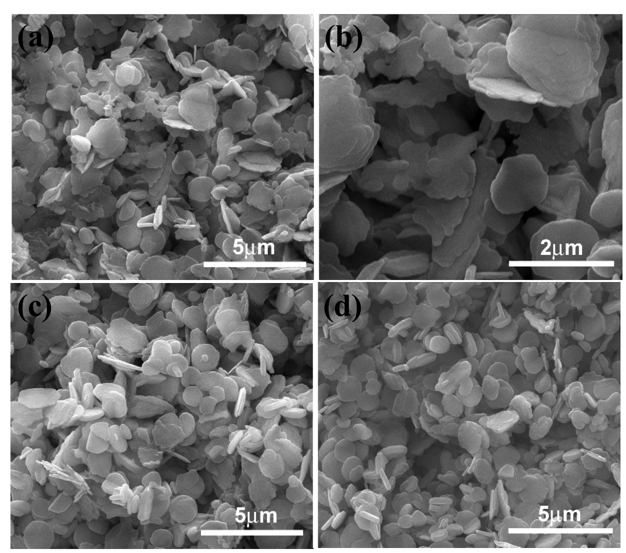

Fig. 5 Low- and high-magnified SEM images of the as-synthesized products collected at different time intervals (a, b) 2 h, (c) 4 h, (d) 6 h.

Fig. 6a shows the charge and discharge curves of the Sn^{4+} doped Fe_2O_3 nanodiscs (0.05% Sn) for the first, second, and five cycles at 100 mA g^{-1} between 0.01 and 3.0 V (vs. Li/Li^+). For the prepared Sn^{4+} doped Fe_2O_3 nanodiscs, the first voltage plateau at approximately 0.9 V may be attributed to the consumption of 1.8 moles Fe_2O_3 in the Li-intercalated process. The second voltage plateau at about 0.75 V indicates the reduction of Fe ions to form nanometer-sized Fe^0 and amorphous Li_2O, and the nanometer-sized Fe^0 can convert to Fe_2O_3 during charge process. Similar results can be observed in the previous reports.[44-46] According to the above discussion, the overall charge-discharge reaction of Fe_2O_3 may be explained in following way:

$$Fe_2O_3+Li^++e^- \leftrightarrow Li_xFe_2O_3\ (x=1.8) \quad (1)$$

$$Li_{1.8}Fe_2O_3+4.2Li^++4.2e^- \leftrightarrow 2Fe+3Li_2O \quad (2)$$

$$2Fe+3Li_2O \leftrightarrow Fe_2O_3+6Li^++6e^- \quad (3)$$

During the discharging process, a high specific capacity of 1390 mAh g-1 is delivered in the 1st Li intercalation process. In the second discharge, the discharge capacity of the electrode decreases to 1005 mAh g-1, which may be attributed to the formation of solid electrolyte interface (SEI) film and further lithium consumption via interfacial reactions due to the charge separation at the metal/Li_2O phase boundary.[47] After 100th cycle, the Fe_2O_3 nanodiscs still deliver a reversible discharge capacity as high as 899 mAh g-1 (Fig. 6b), demonstrating a superior

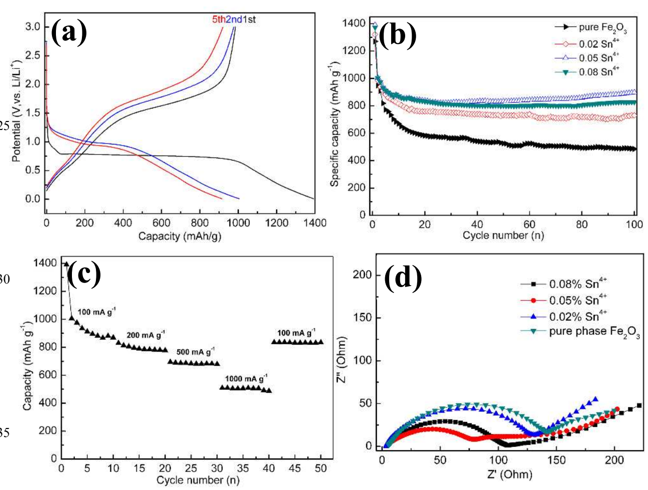

Fig. 6 (a) Charge-discharge voltage profiles of the Sn^{4+} doped Fe_2O_3 nanodiscs electrode for the first, second and fifth cycles at a current density of 100 mA g-1, (b) Cycling performance of the Sn^{4+} doped Fe_2O_3 nanodiscs with different amount of Sn element at the current density of 100 mA g-1, (c) Cycling performance Sn^{4+} Fe_2O_3 electrode at different current rates, (d) Nyquist plots of the Fe_2O_3 nanodiscs.

charge/discharge cycling stability. It should point out that the specific capacity of the electrode decreases slightly during the first 35 cycles and then increases to a constant value. Similar behavior arose from an activation process has been observed in other Fe_2O_3 electrodes.[48-50] They demonstrate that the SEI layer formed during the charge and discharge process, such as ethylene carbonate (EC) and dimethyl carbonate (DMC), and the polymeric gel-type layer. And the layer can alleviate the volume swing of the electrode.[48, 51] Due to the existence of the polymeric gel-type layer, the capacity of Fe_2O_3 nanodiscs increases. In addition, the surface can not be covered by the polymeric layer during the initial cycling stage. That is, the polymeric surface layer builds up slowly during the Li insertion/extraction process. Thus, the discharge capacity of the Sn^{4+} doped Fe_2O_3 nanodiscs increases after 35 cycles. Fig. 6b compares the cycling stability of the Sn^{4+} doped Fe_2O_3 nanodiscs with different amount of Sn element at the current density of 100 mA g-1. As shown in Fig. 6b, the capacity of pure phase Fe_2O_3 electrode decreases slowly to 485 mAh g-1 after 100th cycles. While the Sn^{4+} doped Fe_2O_3 nanodiscs still retain a discharge capacity of over 730 mAh g-1 after 100th cycles. The improvement in cycling stability could be attributed to the introduction of Sn element, which induces much higher conductivity for the electrode. The 5% Sn^{4+} doped Fe_2O_3 nanodiscs shows the highest discharge capacity and cycle stability at 100 mA g-1 among all the samples. Different discharge rates from 100-1000 mA g-1 are applied to investigate the high-rate capability of the samples. The cycling performances of the Sn^{4+} doped Fe_2O_3 nanodiscs (5% Sn) at different current densities are shown in Fig. 6c. Clearly, the capacity gradually degrades with the increase of current density. But cycle specific capacity still remains 490 mAh g-1 at higher current density of 1000 mA g-1. The enhanced electrical conductivity of the electrodes was further verified by EIS measurements. All the electrodes' plots depict a semicircle at middle frequencies region and a straight sloping line in the low frequencies region. The semicircle represents charge-transfer impedance (Rct), while the inclined line is assigned to the lithium-ion diffusion processes (Warburg impedance, W).[52-54] The electrode with smaller the diameter of the semicircle represents the smaller charge transfer resistance. The results in Fig. 6d presents that the addition of Sn element increases the conductivity of the Fe_2O_3 nanodiscs and also decreases the charge-transfer impedance.

4. Conclusions

In summary, Sn^{4+} doped Fe_2O_3 nanodiscs (400 nm in diameter and 100 nm in thickness) have been synthesized under a facile molten salt route. The mechanistic study unravels that the oriented attachment mechanism and the Ostwald ripening process take turns to dominate the fabrication of all the products in different reaction time periods. The investigation of the battery performance shows that the Sn^{4+} doped Fe_2O_3 nanodiscs exhibit a reversible discharge capacity as high as 899 mAh g-1 after 100 cycles at current density of 100 mA g-1, which is much higher than the pure phase Fe_2O_3 nanodiscs (485 mAh g-1). Even at 1000 mA g-1, the reversible capacity of the Sn^{4+} doped Fe_2O_3 nanodiscs could still keep at 490 mAh g-1. Therefore, the Sn doping is an effective approach to achieve excellent electrochemical performance for the Fe_2O_3 anode material.

Acknowledgement

This work was supported by the Natural Science Foundation of China (Project no. 21301086 and 51102128), Natural Science Foundation of Shandong Province (Project no. ZR2013BQ008), and Talent Introduction Fund of Ludong University (Project no. LY2013014).

Notes and references

a School of Chemistry & Materials Science, Ludong University, Yantai 264025, P. R. China. E-mail: jinrc427@126.com; Fax: +86 535 6696162; Tel: +86 535 6696162

b Department of Chemistry, Harbin Institute of Technology, Harbin 150001, P. R. China.

† Electronic Supplementary Information (ESI) available: [details of any supplementary information available should be included here]. See DOI: 10.1039/b000000x/

‡ Footnotes should appear here. These might include comments relevant to but not central to the matter under discussion, limited experimental and spectral data, and crystallographic data.

1 A. Name, B. Name and C. Name, *Journal Title*, 2000, **35**, 3523; A. Name, B. Name and C. Name, *Journal Title*, 2000, **35**, 3523.

1. Y. Idota, T. Kubota, A. Matsufuji, Y. Maekawa and T. Miyasaka, *Science,* 1997, **276**, 1395-1397.
2. W. Wen, J.-M. Wu and M.-H. Cao, *J. Mater. Chem. A*, 2013, **1**, 3881-3885.
3. G.-P. Kim, S. Park, I. Nam, J. Park and J. Yi, *J. Mater. Chem. A*, 2013, **1**, 3872-3876.
4. X. Wang, X.-L. Wu, Y.-G. Guo, Y. Zhong, X. Cao, Y. Ma and J. Yao, *Adv. Funct. Mater.*, 2010, **20**, 1680-1686.
5. Y. Chen, J. Ma, Q. Li and T. Wang, *Nanoscale*, 2013, **5**, 3262-3265.
6. Q.-G. Shao, W.-M. Chen, Z.-H. Wang, L. Qie, L.-X. Yuan, W.-X. Zhang, X.-L. Hu and Y.-H. Huang, *Electrochem. Commun.*, 2011, **13**, 1431-1434.
7. Y. J. Hong, M. Y. Son and Y. C. Kang, *Adv Mater*, 2013, **25**, 2279-2283.
8. J. Ma, X. Zhang, K. Chen, G. Li and X. Han, *J. Mater. Chem. A*, 2013, **1**, 5545-5553
9. M. Y. Son, Y. J. Hong and Y. C. Kang, *Chem. Commun.*, 2013, **49**, 5678-5680.
10. Z. Bai, N. Fan, C. Sun, Z. Ju, C. Guo, J. Yang and Y. Qian, *Nanoscale*, 2013, **5**, 2442-2447.
11. H. Yu, X. Rui, H. Tan, J. Chen, X. Huang, C. Xu, W. Liu, D. Y. W. Yu, H. H. Hng, H. E. Hoster and Q. Yan, *Nanoscale*, 2013, **5**, 4937-4943.
12. X. Sun, Y. Xu, M. Jia, P. Ding, Y. Liu and K. Chen, *J. Mater. Chem. A*, 2013, **1**, 2501-2507.
13. C. Nethravathi, C. R. Rajamathi, M. Rajamathi, U. K. Gautam, X. Wang, D. Golberg and Y. Bando, *ACS Appl. Mater. Interfaces*, 2013, **5** 2708-2714.
14. S.-H. Yu, D. E. Conte, S. Baek, D.-C. Lee, S.-K. Park, K. J. Lee, Y. Piao, Y.-E. Sung and N. Pinna, *Adv. Funct. Mater.*, 2013, **23**, 4293-4305.
15. P. Wang, M. Gao, H. Pan, J. Zhang, C. Liang, J. Wang, P. Zhou and Y. Liu, *J. Power Sources*, 2013, **239**, 466-474.
16. A. Bhaskar, M. Deepa and T. N. Rao, *ACS Appl. Mater. Interfaces*, 2013, **5** 2555-2566.
17. L.-L. Xing, C.-X. Cui, P. Deng, Y.-X. Nie, Y.-Y. Zhao, B. He and X.-Y. Xue, *RSC Adv.*, 2013, **3**, 10379-10384.
18. Q.-q. Xiong, J.-p. Tu, X.-h. Xia, X.-y. Zhao, C.-d. Gu and X.-l. Wang, *Nanoscale*, 2013, **5**, 7906-7912.
19. Y. Feng, R. Zou, D. Xia, L. Liu and X. Wang, *J. Mater. Chem. A*, 2013, **1**, 9654-9658.
20. C. Wu, P. Yin, X. Zhu, C. Ou Yang and Y. Xie, *J. Phys. Chem. B*, 2006, **110**, 17806-17812.
21. B. T. Hang, S. Okada and J. Yamaki, *J. Power Sources*, 2008, **178**, 402–408.
22. J. Chen, L. Xu, W. Li and X. Gou, *Adv. Mater.*, 2005, **17**, 582-586.
23. Y. Jiang, D. Zhang, Y. Li, T. Yuan, N. Bahlawane, C. Liang, W. Sun, Y. Lu and M. Yan, *Nano Energy*, 2014, **4**, 23-30.
24. A. S. Arico, P. Bruce, B. Scrosati, J. M. Tarascon and W. V. Schalkwijk, *Nat. Mater.* 2005, **4**, 366-377.
25. Y. G. Zhu, J. Xie, G. S. Cao, T. J. Zhu and X. B. Zhao, *RSC Adv.*, 2013, **3**, 6787-6793.
26. F. Zhang, T. Zhang, X. Yang, L. Zhang, K. Leng, Y. Huang and Y. Chen, *Energy Environ. Sci.*, 2013, **6**, 1623-1632.
27. J. Balach, H. Wu, F. Polzer, H. Kirmse, Q. Zhao, Z. Wei and J. Yuan, *RSC Adv.*, 2013, **3**, 7979-7986.
28. W. Zhou, L. Lin, W. Wei, H. Jin, J. Li and L. Guo, *RSC Adv.*, 2013, **3**, 7933-7937.
29. A. G. Nasibulin, S. Rackauskas, H. Jiang, Y. Tian, P. R. Mudimela, S. D. Shandakov, L. I. Nasibulina, J. Sainio and E. I. Kauppinen, *Nano Res.*, 2009, **2**, 373-379.
30. K. K. Lee, S. Deng, H. M. Fan, S. Mhaisalkar, H. R. Tan, E. S. Tok, K. P. Loh, W. S. Chin and C. H. Sow, *Nanoscale*, 2012, **4**, 2958-2961.
31. X. Qi, G. She, M. Wang, L. Mu and W. Shi, *Chem. Commun.*, 2013, **49**, 5742-5744.
32. J. Ma, T. Wang, X. Duan, J. Lian, Z. Liu and W. Zheng, *Nanoscale*, 2011, **3**, 4372-4375.
33. L. Wang, J. Ma, L. Chen, Z. Xu and T. Wang, *Electrochim. Acta* 2013, **113**, 194-199.
34. J. Lu, Q. Peng, Z. Wang, C. Nan, L. Li and Y. Li, *J. Mater. Chem. A*, 2013, **1**, 5232-5237.
35. M.V. Reddy, C. T. Cherian, K. Ramanathan, K. C. W. Jie, T. Y. W. Daryl, T. Y. Hao, A. S., K. P. Loh and B. V. R. Chowdari, *Electrochim. Acta*, 2014, **118**, 75-80.
36. M. V. Reddy, C. Yu, F. Jiahuan, K. P. Loh and B. V. R. Chowdari, *ACS Appl. Mater. Interfaces*, 2013, **5**, 4361-4366.
37. M. V. Reddy, Z. Beichen, K. P. Loh and B. V. R. Chowdari, *CrystEngComm*, 2013, **15**, 3568-3574.
38. M. V. Reddy, L. Y. T. Andreea, A. Y. Ling, J. N. C. Hwee, C. A. Lin, S. Admas, K. P. Loh, M. K. Mathe, K. I. Ozoemena and B. V. R. Chowdari, *Electrochim. Acta* 2013, **106**, 143- 148.
39. M. V. Reddy, S. Adams, G. T. J. Liang, I. FooMingze, H. V. T. An and B. V. R. Chowdari, *Solid State Ionics*, 2014, **262** 120-123.
40. M. V. Reddy, K. Y. H. Kenrick, T. Y. Wei, G. Y. Chong, G. H. Leong and B. V. R. Chowdari, *J. Electrochem. Soc.*, 2011, **158** A1423-A1430
41. M. V. Reddy, C. Yu, F. Jiahuan, K. P. Loh and B. V. R. Chowdari, *RSC Adv.*, 2012, **2**, 9619-9625.
42. H. Lv, L. Ma, P. Zeng, D. Ke and T. Peng, *J. Mater. Chem.*, 2010, **20**, 3665-3672.
43. R. Liu, S. Yang, F. Wang, X. Lu, Z. Yang and B. Ding, *ACS Appl. Mater. Interfaces*, 2012, **4**, 1537-1542.
44. M. V. Reddy, G. V. Subba Rao and B. V. R. Chowdari, Chem. Rev., **113**, 5364-5457.
45. M. V. Reddy, T. Yu, C.-H. Sow, Z. X. Shen, C. T. Lim, G. V. Subba Rao and B. V. R. Chowdari, *Adv. Funct. Mater.*, 2007, **17**, 2792-2799.
46. C. T. Cherian, J. Sundaramurthy, M. Kalaivani, P. Ragupathy, P. Suresh Kumar, V. Thavasi, M. V. Reddy, C. H. Sow, S. G. Mhaisalkar, S. Ramakrishna and B. V. R. Chowdari, *J Mater Chem.*, 2012, **22**, 12198-12204.
47. G. Gao, Q. Zhang, K. Wang, H. Song, P. Qiu and D. Cui, *Nano Energy*, 2013, **2**, 1010-1018.

48. J. Zhu, Z. Yin, D. Yang, T. Sun, H. Yu, H. E. Hoster, H. H. Hng, H. Zhang and Q. Yan, *Energy Environ. Sci.*, 2013, **6**, 987-993.
49. J. Zhu, T. Zhu, X. Zhou, Y. Zhang, X. W. Lou, X. Chen, H. Zhang, H. H. Hng and Q. Yan, *Nanoscale*, 2011, **3**, 1084-1089
50. Y.-M. Lin, P. R. Abel, A. Heller and C. B. Mullins, *J. Phys. Chem. Lett.* , 2011, **2**, 2885-2891.
51. X. Wang, X.-L. Wu, Y.-G. Guo, Y. Zhong, X. Cao, Y. Ma and J. Yao, *Adv. Funct. Mater.*, 2010, **20**, 1680-1686. .
52. N. Sharma, J. Plevert, G. V. Subba Rao, B. V. R. Chowdari and T. J. White, *Chem. Mater.*, 2005, **17**, 4700.
53. M. S. Park, Y. M. Kang, G. X. Wang, S. X. Dou and H. K. Liu, *Adv. Funct. Mater.*, 2008, **18**, 455.
54. H. Shu, X. Wang, Q. Wu, B. Hu, X. Yang, Q. Wei, Q. Liang, Y. Bai, M. Zhou, C. Wu, M. Chen, A. Wang and L. Jiang, *J. Power Sources*, 2013, **237**, 149-155.

TOC

Sn^{4+} doped α-Fe_2O_3 nanodiscks with good lithium storage properties have been prepared by a melton salt method.